Percolation of CO2-rich fluids in a limestone sample: Evolution of hydraulic, electrical, chemical, and structural properties

Stéphanie Vialle, Simon Contraires, Bernard Zinzsner, Jean-Baptiste Clavaud, Karim Mahiouz, Pierpaolo Zuddas, Maria Zamora

AGU PUBLICATIONS

JGR

Journal of Geophysical Research: Solid Earth

RESEARCH ARTICLE
10.1002/2013JB010656

Key Points:
- Percolation experiments of CO2-rich fluids on a well-characterized limestone
- X-rays tomography shows the formation of wormholes
- Non-seismic geophysical monitoring is suitable in chemical reactive systems

Correspondence to:
S. Vialle,
svialle@stanford.edu

Citation:
Vialle, S., S. Contraires, B. Zinzsner, J.-B. Clavaud, K. Mahiouz, P. Zuddas, and M. Zamora (2014), Percolation of CO_2-rich fluids in a limestone sample: Evolution of hydraulic, electrical, chemical, and structural properties, *J. Geophys. Res. Solid Earth*, *119*, 2828–2847, doi:10.1002/2013JB010656.

Received 31 AUG 2013
Accepted 9 MAR 2014
Published online 15 APR 2014

Percolation of CO_2-rich fluids in a limestone sample: Evolution of hydraulic, electrical, chemical, and structural properties

Stéphanie Vialle[1,2], Simon Contraires[1], Bernard Zinzsner[1], Jean-Baptiste Clavaud[1,3], Karim Mahiouz[1,4], Pierpaolo Zuddas[5], and Maria Zamora[1]

[1]Institut de Physique du Globe de Paris, Sorbonne Paris Cité, Université Paris Diderot, Paris, France, [2]Now at Earth Sciences Division, Lawrence Berkeley National Laboratory, Berkeley, California, USA, [3]Now at Chevron Energy Technology Company, Houston, Texas, USA, [4]Now at CNRS-DT INSU, La Seyne sur Mer, France, [5]Institut des Sciences de la Terre, UPMC-Sorbonne Universités, Paris, France

Abstract Percolation of CO_2-rich fluids in limestones causes the dissolution (and eventual reprecipitation) of calcium carbonate minerals, which affect the rock microstructure and change the rock petrophysical properties (i.e., hydraulic, electrical, and elastic properties). In addition, microstructural changes further feed back to affect the chemical reactions. To better understand this coupled problem and to assess the possibility of geophysical monitoring, we performed reactive percolation laboratory experiments on a well-characterized carbonate sample 35 cm in length and 10 cm in diameter. In a comprehensive study, we present integrated measurements of aqueous chemistry (pH, calcium concentration, and total alkalinity), petrophysical properties (permeability, electrical formation factor, and acoustic velocities), and X-ray tomography imaging. The measured chemical and electrical parameters allowed rapid detection of the dissolution of calcite in the downstream fluid. After circulating fluids of various salinities at 5mL min^{-1} for 32 days (about 290 pore sample volumes) at a pCO_2 of 1 atm (pH = 4), porosity increased by 7% (from 0.29 to 0.31), permeability increased by 1 order of magnitude (from 0.12 D to 0.97 D), and the electrical formation factor decreased by 15% (from 15.7 to 13.3). X-ray microtomography revealed the creation of wormholes; these, along with the convex curvature of the permeability-porosity relationship, are consistent with a transport-controlled dissolution regime for which advection processes are greater than diffusion processes, confirming results from previous numerical studies. This study shows that nonseismic geophysical techniques (i.e., electrical measurements) are promising for monitoring geochemical changes within the subsurface due to fluid-rock interactions.

1. Introduction

The chemical reactions between a fluid and the porous medium through which it flows are of fundamental and practical importance in many scientific, industrial, or engineering problems. Dissolution and precipitation are important processes, because they affect the groundwater chemistry and can significantly modify the microstructure of the porous medium [e.g., *Hoefner and Fogler*, 1988; *Noiriel et al.*, 2005], and, as a consequence, its macroscopic parameters including hydraulic properties [*Rege and Fogler*, 1989; *Békri et al.*, 1995; *Tenthorey et al.*, 1998; *Ormond and Ortoleva*, 2000; *Clavaud*, 2001; *Singurindy and Berkowitz*, 2003; *Noiriel et al.*, 2005, 2007; *Vialle*, 2008], electrical properties [*Guichet et al.*, 2003; *Abdel Aal et al.*, 2009], and elastic rock properties [*Contraires et al.*, 2007; *Le Guen et al.*, 2007; *Contraires*, 2008; *Vanorio et al.*, 2008, 2010; *Vialle and Vanorio*, 2011]. Dissolution and precipitation may also feedback upon themselves, affecting the subsequent fluid-rock interactions [*Polak et al.*, 2004].

There is a vast literature analyzing the influences of dissolution and precipitation on the hydraulic, electric or textural evolution of rock properties, and a broad range of theoretical, numerical, laboratory, and field investigations have been undertaken. Among the media that have been studied, carbonate rocks are particularly important, not only because these are the most abundant rocks at the surface but also because—due to their high dissolution rate [*Langmuir*, 1971; *Sigg et al.*, 1994]—they are particularly reactive. As a result, they play a major role in numerous fields: global geochemical cycles, diagenesis of sediments and sedimentary rocks [*Machel*, 1999], impact of acid rain on the decay of buildings in urban environments [*Viles*, 1997; *Viles and*

Moses, 1998; *Bravo et al.*, 2006], petroleum reservoir characteristics [*Rege and Fogler*, 1989], acid leaching from sanitary landfills and mining waste rock [*Eriksson and Destouni*, 1997], intrusion of saline groundwater in coastal environments [*Plummer*, 1975; *Back et al.*, 1979; *Higgins*, 1980; *Smart et al.*, 1988; *Price and Herman*, 1991; *Singurindy and Berkowitz*, 2003; *Rezaei et al.*, 2005], storage and recovery of water [*Cederstrom*, 1957; *Gale et al.*, 2002], and geological sequestration of CO_2 [e.g., *Noiriel et al.*, 2005; *Sterpenich et al.*, 2009; *Luquot and Gouze*, 2009; *Vialle and Vanorio*, 2011]

It is well known that the flow through a soluble porous medium may lead to heterogeneous dissolution and to the formation of channel-like altered areas, usually referred to as "wormholes" [e.g., *Nougaro and Labbe*, 1955; *Hoefner and Fogler*, 1988]. The oil and gas industry uses so-called stimulation treatments, injecting acid into wells to dissolve part of the porous medium and increase permeability near the wellbore, to enhance oil and gas production. In the near-wellbore area, high flow rates and unbalanced geochemical reactions should lead to localized dissolution patterns and wormhole growth [*Bazin*, 2001; *Egermann et al.*, 2005], whereas dissolution is expected to be more homogeneous farther from the well [*André et al.*, 2007]. Karsts are the example of heterogeneous and massive dissolutions by subsurface flow at a regional scale [e.g., *White*, 1988]. Many laboratory and numerical experiments of dissolution have been performed in a variety of fluid-carbonate systems [e.g., *Nougaro and Labbe*, 1955; *Hoefner and Fogler*, 1988; *Renard et al.*, 1998]. All conclude that the development of different dissolution regimes (compact wormholes, ramified wormholes, and uniform dissolution) depends on various controlling factors, such as injection rates, the nature of the acid, the initial microstructure, the initial presence of clay minerals, and the presence of fracture. The physics of porous media dissolution and wormhole formation is now quite well understood, and many qualitative and quantitative models have been proposed to explain these processes, which have been identified as nonlinear processes of self-organization, based on positive feedback loops [*Ormond and Ortoleva*, 2000]. While models were mainly qualitative at first, *Golfier et al.* [2002] proposed the first quantitative and comprehensive model, a three-dimensional coupled reaction-transport Darcy-scale model that reproduces all the dissolution regimes observed in the literature. The mechanism of wormhole propagation is treated as an unstable phenomenon that depends on the rock microscopic properties at the pore scale and is controlled by the injection rate of the fluid, which is quantified by two dimensionless numbers, the Péclet and Damkhöler numbers. They represent the magnitude of the convective transport versus the diffusional transport and the magnitude of the dissolution reaction versus the convective transport, respectively.

A few experimental and numerical studies have investigated the relationship between the dissolution and precipitation processes, the created dissolution pattern and the evolution of the hydraulic conductivity [e.g., *Mc Cune et al.*, 1979; *Békri et al.*, 1995; *Singurindy and Berkowitz*, 2003; *Noiriel et al.*, 2005; *Gouze and Luquot*, 2011]. The systematic numerical study of *Békri et al.* [1995] shows that different dissolution regimes (and thus different generated dissolution patterns) lead to different and characteristic permeability-porosity relationships, in tune with laboratory results.

Despite all of these studies, little has been done to identify, develop, and test geophysical methods able to monitor from the surface dissolution and precipitation processes that occur inside the porous media. *Guichet et al.* [2006] show that the precipitation of calcite as a secondary mineral phase in a quartz-calcite sand, reducing permeability, has a significant effect on the measured spontaneous potential (SP). This result may help incorporate SP anomalies in hydrothermal fields with mineralogical analyses of hydrothermal deposits and geochemical fluid surveys to infer fluid circulation patterns. Dissolution and precipitation of carbonate minerals also affect the seismic response of the host rock [e.g., *Contraires et al.*, 2007; *Contraires*, 2008; *Vanorio et al.*, 2008, 2010; *Vialle and Vanorio*, 2011], rendering the traditional rock-physics models, which do not take into account any fluid-rock interactions, inadequate [*Vanorio et al.*, 2008, 2010].

The main aim of the experimental work in this paper is to better understand the relationship between the dissolution of a natural porous limestone and the change in its physical parameters, namely permeability, electrical conductivity P and S wave velocities. We perform reactive percolation experiments on a limestone. We carefully characterize sample microstructure and physical properties (hydraulic, electrical, and elastic) before and after the percolation experiments, using various techniques. During the experiments, we continuously monitor both the chemical parameters (pH, calcium content, and total alkalinity) and the physical ones (permeability, electrical formation factor, and ultrasonic velocities).

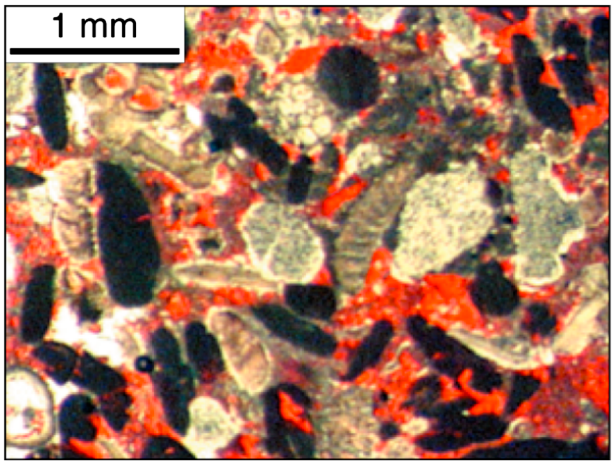

Figure 1. Thin section of the studied carbonate sample from Estaillades (France). The pore space is filled with red epoxy.

2. Materials and Methods

2.1. Sample Characterization

The rock chosen for this study is a bioclastic limestone (Estaillades limestone, France), composed of more than 99% calcite. The grain size ranges from 0.5 to 1 mm (Figure 1). Intergranular macroporosity is important and is sometimes obstructed by microcrystals of calcite (i.e., micrite). The microporosity is important in the bioclasts (algae).

The sample is a cylinder 10 cm in diameter and 35 cm long. This scale is larger than the homogenization scale of the rock [e.g., *Youssef et al.*, 2007] and 1 order of magnitude larger than the usual size in laboratory percolation experiments. This size makes it possible to study the effect of the heterogeneity of the rock. The sample was coated with an epoxy resin to render its boundaries impermeable. The impermeability of the coating was verified by putting the sample under vacuum conditions for a few hours.

Before and after the experiments, we carefully characterized the sample using different techniques to determine porosity, permeability, pore-throat radius distribution, and information about the sample heterogeneities.

Porosity and absolute water permeability were measured using a macropermeameter [*Clavaud*, 2001] designed to measure porosity, absolute permeability, and electrical conductivities of large samples, as well as the conductivity of the solution saturating the sample. This apparatus allows miscible displacements as well. The sample was first saturated under vacuum with distilled and degassed water to measure the connected porosity of the sample, which is the ratio between the volume of injected water (V_{inj}) and the total volume of the sample (V_t). After porosity measurement, absolute water permeability (k_w) was obtained by injecting distilled water with a constant pressure drop of 23 kPa across the sample. The flow rate was monitored at the sample outlet, and absolute water permeability was obtained by Darcy equation [*Darcy*, 1856].

Pore-throat radius distribution was measured by Mercury Injection Capillary Pressure tests on a cylinder of 1 cm in diameter and 2 cm in length taken in the same block as the studied sample. The pressure used during the measurements ranged from 2×10^{-3} to 150 MPa, which corresponds to a range of measurable pore-throat radii from 350 μm to 0.0025 μm.

2.2. Characterization of the Heterogeneity of the Sample

Information about the sample heterogeneities were obtained before and after the experiment using (a) miscible displacements experiments, (b) ultrasonic *P* and *S* wave velocity measurements along the main axis of the sample, and (c) X-ray tomography.

2.2.1. Miscible Displacements Experiments

We used miscible displacement experiments to get information about the heterogeneity of the rock and the existence of preferential circulation paths. Brine (a 25 g L^{-1} NaCl solution) was injected in the sample initially filled with distilled water, and electrical conductivities of the rock and of the fluid at the outlet were monitored until the conductivity of the effluent persistently matched that of the injected brine. The rock and fluid electrical conductivities, normalized to their final values, were then plotted as a function of injected pore volume of fluids. The obtained curves, the so-called breakthrough curves, do not show a sharp change in conductivity when the high-conductivity brine arrives at the sample outlet, but a gradual change due to a gradual mixing of the two solutions resulting from hydrodynamic dispersion. Hydrodynamic dispersion results from the microscopic nonuniformity of flow velocities in the conducting pores and is thus linked to the heterogeneities of the sample pore system. Two parameters were determined from this experiment: the "stability volume" (SV), which is the volume of injected brine (expressed in number of pore volumes) required

to reach a stable electrical conductivity, and the "electrical percolation threshold" (EPT), defined as the fraction of invaded pore volume at which the sample conductivity departs from its initial value of 4×10^{-5} S/m. An EPT close to 1 indicates that the fluid moves as a uniform front, whereas a low EPT indicates that brine uses preferential pathways. Values were deduced from the fluid conductivity curve. We can detect more precisely the first brine arrival (i.e., the "breakthrough") [e.g., *Dullien*, 1992] and constrain the stability volume on that curve. If a small area of the pore system remains saturated with distilled water, it is difficult to detect it using the bulk sample electrical conductivity, whereas it is clearly apparent on the effluent conductivity curve.

Since the studied sample contains no clays, and since the injected brine has a high salinity, the surface and the matrix electrical conductivities are negligible [*Johnson and Sen*, 1988; *Garrouch and Sharma*, 1994] compared to that of the brine. In these conditions, the electrical formation factor (F) can be approximated by

$$F = \frac{\sigma_f}{\sigma_s}, \tag{1}$$

where σ_s is the sample conductivity and σ_f is the brine conductivity, both measured at the end of the miscible displacement experiment. Measurements of the sample electrical conductivity were performed with a two-pole electrode technique, at frequencies ranging from 100 Hz to 100 kHz, chosen to minimize the electrode polarization. During the measurements, the sample was placed between two stainless steel electrodes connected to an impedance meter (HP4263A). The brine conductivity was measured with an in-line conductivity cell (TetraCon DU/T). The experimental uncertainty is less than 1% and 0.5% for the rock and fluid conductivities, respectively.

The cementation factor, m, was then deduced from Archie law:

$$F = \phi^{-m}, \tag{2}$$

in which ϕ is the porosity of the sample, and the electrical tortuosity, τ_e, is from the following relation [*Wyllie*, 1957]:

$$\tau_e^2 = F\,\phi. \tag{3}$$

2.2.2. Ultrasonic *P* and *S* Wave Measurements

To determine the longitudinal heterogeneity of the sample, compressional (P) and shear (S) wave velocities were measured across three diameters of the cylindrical core sample, spaced every centimeter along its length. Ultrasonic velocities at 1 MHz were obtained by using a pulse-transmission technique [*Birch*, 1960] with a high-viscosity bonding medium that ensures good coupling between the sample and the transducers (Panametrics V103SB for P waves and V153SB for S waves). Details can be found in *Zamora and Poirier* [1990]. Measurements were made at atmospheric pressure and room temperature on both dry and saturated samples. The measurement uncertainties associated with velocities are estimated to be less than 2 %.

2.2.3. X-Ray Tomography

X-ray tomography was performed on the studied core before and after the injecton experiments. This nondestructive method is based on the measurement of X-ray attenuation by the sample. Measurements were carried out in a medical scanner (CE12000), and a radial slice was obtained every 1 mm along the core axes, at a pixel-size resolution of 0.09 mm. The obtained CT images display attenuation, represented by gray-scale variations that depend on the thickness of the sample, the mineralogy, and the spatial variation of the rock matrix density.

2.3. Experimental Procedures

2.3.1. Injection Experiment

We injected an acidic fluid (a CO_2-rich solution) that could chemically react with the rock and monitored the effects on porosity, permeability, electrical formation factor, P and S wave velocities, and chemistry of the output fluid.

The carbonate sample, saturated under vacuum with distilled water before the experiment, was flooded at a constant flow rate of 5 mL min^{-1}. The experiment lasted several months, with two equilibration periods (noted NI) and three phases of fluid injection (labeled 1, 2, and 3). Three types of fluid were injected: distilled water with sodium chloride NaCl at a concentration of 10^{-2} mol L^{-1} and pH of about 6 (called fluid S), the same fluid saturated with CO_2 at a partial pressure of 0.1 MPa, decreasing the pH to about 4 (fluid SC), and distilled water saturated with CO_2 at the same partial pressure (fluid DC). Figure 2 shows the experimental

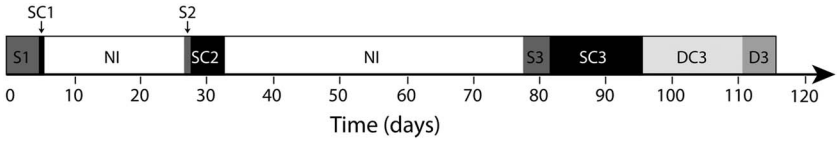

Figure 2. Timeline of the different phases of the percolation experiments carried out on the studied carbonate sample, color coded by fluid type (see text for the meaning of the abbreviations and Table 1 for the details). NI stands for "No Injection."

timeline, and the pH and electrical conductivities of the fluids are specified in Table 1. The experiment was carried out at room temperature. This sequence of injections allowed us to study (1) the effect of the dissolved CO_2 on the microstructure and rock properties of the studied carbonate, by injecting the same brine, without and then with CO_2 (e.g., injection S1 followed by SC1, or S2 followed by SC2, S3 followed by SC3); and (2) the effect of salinity, by injecting distilled water just after the brine, both fluids having the same partial pressure of CO_2 (injection SC3 followed by DC3). The last injection of pure distilled water, D3, was meant to remove any reactive fluid and fluid enriched in dissolved calcite, before drying the rock and carrying out the microstructural characterizations and rock properties measurements. Letting a fluid enriched in dissolved calcite in the pore space during drying would have led to secondary precipitation of calcite. The first phase of injections was short, meant to test that the methodology and the experimental device were working properly. Before proceeding with the next phase of injection, the results were carefully analyzed to detect any problem, either in the acquisition of the different parameters or in the device itself (eventual leaks for example). Similarly, the phase 2 of injection was stopped after a few days (period of no injection NI) to analyze the data before proceeding with the last sequence of injection.

2.3.2. Experimental Device

Figure 3 is a schematic drawing of the experimental device. This apparatus allows us to monitor the permeability (k), the electrical formation factor (F), and the chemical composition of the output fluid. The fluid injection line includes several in-line sensors: a water conductimeter (TetraCon DU/T), to measure the water conductivity σ_w, a pH meter (Scientific Instrument Consort P 500) at the outlet, two pressure gauges (Aschcrof KXD) to measure the fluid pressure P_1 and P_2 at the inlet and outlet, respectively, a flow meter (McMillan 106 FloSensor) to measure the flow rate Q, and a thermocouple (Cole Parmer Instrument) to measure the fluid temperature T. A main reservoir contains the fluid to be injected. A pump (Gilson Minipuls 3) was used to inject the solution through the sample at a constant rate, and two valves allow sampling of the solution at the inlet and the outlet of the sample. The connections between the different elements are made of PVC tubes, and the joins are ABS (Acrylonitrile butadiene styrene). The sample is placed in a core holder (Figure 3) with two endcaps, each containing a stainless steel electrode, a PVC cap (for electrical isolation), and a metal sheet to ensure good contact between the sample and the electrodes. The electrical conductivity of the sample was measured on an HP 42263A impedance meter.

Table 1. Chronology of the Experiment, Indicating the Starting Day of the Period, Its Name, the pH of the Injected Fluid, and Its Electrical Conductivity σ_f[a]

Day	Period	pH	σ_f (S/m)
0	S1	6.09	0.10
5	SC1	4.02	0.10
6 to 26		No Injection	
27	S2	5.98	0.10
28	SC2	3.88	0.10
32 to 77		No Injection	
78	S3	6.02	0.10
82	SC3	4.03	0.10
96	DC3	4.03	4.0×10^{-5}
110	D3	5.96	3.8×10^{-5}
112		End of the experiment	

[a]The name of the period refers to the type of injected fluid: S for distilled water containing salt (NaCl), SC for distilled water containing salt and saturated with CO_2, D for pure distilled water, and DC for distilled water saturated with CO_2.

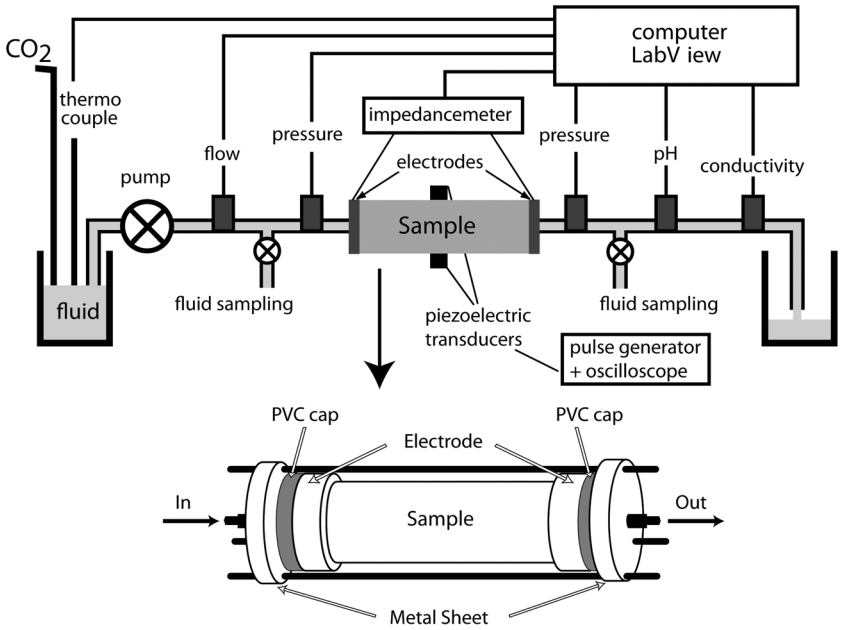

Figure 3. (top) Schematic drawing of the experimental device used for the reactive percolation experiments. (bottom) Detailed view of the sample core holder.

2.3.3. Monitored Parameters

All the parameters were automatically recorded on a computer and visualized during the test using LabView software developed for this purpose. The electrical formation factor was calculated by equation (1) and the permeability, k, by the Darcy equation

$$k = \frac{\mu Q L}{S \Delta P}, \tag{4}$$

where μ is the fluid viscosity (Pa s), Q is the flow rate ($m^3\,s^{-1}$), L and S are the length (m), and the cross section (m^2) of the sample, respectively, and $\Delta P = (P_{out} - P_{in})$ is the pressure difference across the sample.

During the experiment, the fluid was regularly sampled at the outlet after its passage through the sample and filtered at 0.2 μm. Calcium concentration was determined by titration and alkalinity, which is defined as the capacity of a solution to neutralize acids [*Sigg et al.*, 1994], by spectrophotometry. A complete ion content analysis by ionic chromatography was also performed on some of the samples, both to check the accuracy and reliability of the titration and spectrophotometry measurements and to confirm that calcium was the major dissolved cation (not present in the injected fluid). All the samples subjected to cation analysis (calcium from titration or cations from ionic chromatography) were acidified with two drops of concentrated HNO_3.

Calcium concentration was determined by complexometric titration using Ethylenediaminetetraacetic acid (EDTA) as titrant solution and the Digital Titrator HACH LANGE® 1690. The end point was determined by colorimetry (HACH® method 8204 of the user's manual). The maximum experimental uncertainty in the calcium concentrations varies according to the volume of the fluid sample and the concentration of the EDTA solution; these are functions of the expected calcium concentration, which ranges from 3% to 5.5%.

Alkalinity was determined by an analytical procedure adapted from the method proposed by *Podda and Michard* [1994]. It consists in neutralizing all the basic species by a weak acid (methanoïc acid, HCOOH) mixed with a pH-sensitive dye (bromo-phenol blue) that has a dissociation constant close to that of the methanoïc acid. The neutralization leads to a final mixture having an absorbance at 590 nm that is a function of the original alkalinity of the sample. The absorbance at 590 nm is read on a single-beam spectrophotometer Lovibond. A complete description of the method is given in *Sarazin et al.* [1999]. The experimental uncertainty has been estimated to be less than 5%.

Table 2. Equations Proposed by *Plummer and Busenberg* [1982] for the Carbonate System in Equilibrium With Calcite in Aqueous Media[a]

Equation	Log K (25°C)
$CO_2 + H_2O \Leftrightarrow H2CO3$	−1.47
$H_2CO_3 \Leftrightarrow H^+ + HCO_3^-$	−6.35
$HCO_3^- \Leftrightarrow H^+ + CO_3^{2-}$	−10.33
$Ca^{2+} + CO_3^{2-} \Leftrightarrow CaCO_3$	−8.42

[a]The values of the associated thermodynamic constants are the ones at 25°C.

Other ions were analyzed by ionic chromatography on a DIONEX™ 120 chromatograph. The concentrations were obtained with an accuracy of 4% to 5%. These values are comparable to the ones obtained with the digital titrator, the latter having the advantage to give concentrations a few minutes after sampling.

2.3.4. Quantification of Calcite Dissolution

From the parameters measured during the injection experiments, we evaluated the degree of saturation of calcite, the global rate of calcite dissolution and the change in porosity due to the dissolution of calcite. We used the set of equations and the associated thermodynamic constants proposed by *Plummer and Busenberg* [1982] (Table 2) for a carbonate system in equilibrium with calcite in an aqueous medium. The values are given at 25°C.

The degree of saturation of calcite is defined as

$$\Omega = \frac{(Ca^{2+})(CO_3^{2+})}{K_{sp}}, \tag{5}$$

where (Ca^{2+}) and $(CO_3{}^{2-})$ are the activities (measured concentrations times the activity coefficients γ_i) of the calcium and the carbonate ions in the solution, respectively, and K_{sp} is the thermodynamic solubility product of calcite. The activity coefficients γ_2 have been calculated with the Davies formula valid for an ionic strength less than 0.5 mol L^{-1}. The ionic strength I has been calculated from the electrical conductivity measured in the outlet effluent, with the help of the Talbot formula, valid in the limits of the Güntelberg theory (i.e., $I < 0.1$ mol L^{-1}):

$$I = 10^{-3}(0.0021 + 0.148\ \sigma_f). \tag{6}$$

Here σ_f is in mS cm^{-1} and I is in mol L^{-1}.

Since the studied system contains no acids or bases other than the ones of the carbonate system, and since the pH measured in the output fluid is around 6, alkalinity can be approximated by the concentration of the bicarbonate ion, and the calcite saturation degree can be thus rewritten as

$$\Omega = \frac{[Ca^{2+}]\ \mathrm{Alk}\ K_2\ \gamma_2^2}{K_{sp}\ 10^{pH}}. \tag{7}$$

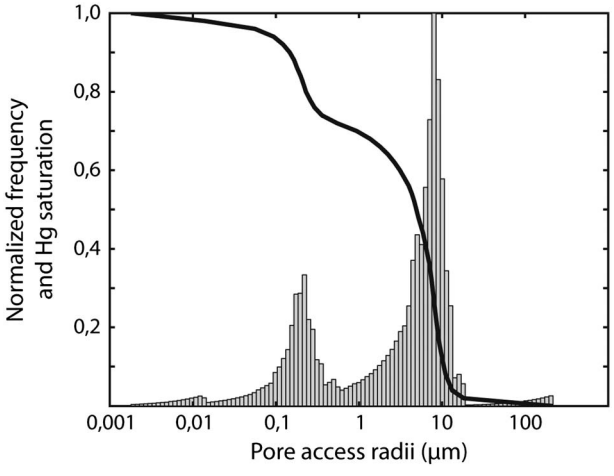

Figure 4. Pore-throat distribution (histogram) and mercury capillary curve as a function of pore-throat radius (solid line). The capillary curve is expressed in mercury saturation, which is the volume of mercury injected in the sample divided by its final value. The pore-throat distribution is clearly bimodal.

Using mass balances and the fact that the rock is composed of nearly pure calcite, the variation of porosity over the time interval $[t_i; t_{i+1}]$, is given by

$$\Delta\phi(t_i) = \frac{Q\ M_{CaCO_3}\ \overline{[Ca^{2+}]}_i}{V_s\ \rho_{CaCO_3}}, \tag{8}$$

where M_{CaCO3} is the molecular weight of calcium carbonate, $\overline{[Ca^{2+}]}_i$ is the average calcium concentration over the time interval $[t_i; t_{i+1}]$ and ρ_{CaCO3} is calcite density.

3. Results

3.1. Sample Properties Before the Reactive Percolation Experiment

Porosity and permeability of the sample before the injections experiments were 28.6 ± 0.3% and 0.12 ± 0.07 D, respectively.

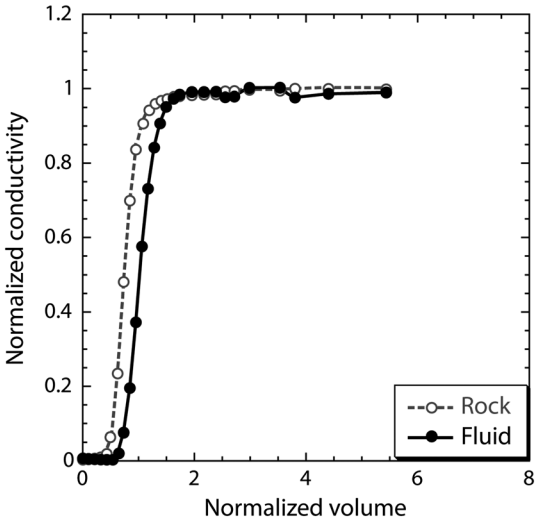

Figure 5. Results of the miscible displacement experiment before the percolation experiments. The electrical conductivities of the rock and of the fluid (normalized to their final values) are plotted as functions of the injected volume of brine (normalized to the sample pore volume).

Figure 4 shows that the pore-throat radius distribution is bimodal, with two maxima at 8 μm and 0.20 μm, and pore-throat radii ranging from 250 to 8×10^{-3} μm.

Figure 5 shows the evolution of the electrical conductivities of the sample and of the effluent (both normalized to their final values) as functions of the volume of injected brine (normalized to the sample pore volume). The inferred stability volume and the electrical percolation threshold are 2.2 and 0.3, respectively. These values indicate that the sample is heterogeneous and that it most likely contains some preferential pathways. The electrical formation factor, the Archie cementation factor, and the electrical tortuosity obtained at the end of the miscible displacement are 15.7, 2.2, and 2.1 respectively.

Figure 6 presents the mean *P* and *S* wave velocities (V_{PM} and V_{SM}), obtained from the measurements performed along three diameters of the sample at 60° from each other, and the radiological density (DR), as a function of the position along the length of the sample, both in dry conditions. The mean *P* wave velocities range from 3110 m s^{-1} to 3638 m s^{-1}, and the mean *S* wave range from 1806 m s^{-1} to 2115 m s^{-1}. The evolution of the radiological density along of the sample, ranging from 1349 UH to 1502 UH, follows a similar trend as the *P* and *S* wave velocities. Three main zones can be observed: the first one (in the 10 first cm) has high values of both *P* and *S* wave velocities and radiological density; the second one (between 10 and 20 cm) has lower values, and the third one has values similar to the first zone. The sample is clearly heterogeneous lengthwise. *P* and *S* wave measurements and X-ray tomography thus provide similar information about the longitudinal heterogeneity of the sample (Figure 6); however, velocity measurements can be made in situ; they will be the measure used during the percolation experiment.

3.2. Effects of the Injection of a CO_2-Enriched Fluid

Figure 7 shows the evolution of the different parameters measured during the first day of the second injection of the CO_2-enriched fluid (Figure 2, periods S2 and SC2). Similar behaviors were observed for all three injections. The values of alkalinity, calcium concentration, fluid electrical conductivity, and pH show a rapid and significant change about 2 h after the beginning the CO_2-rich fluid injection. This period (highlighted in Figure 7, dark grey) corresponds to the time needed for the fluid to react with the calcite composing the rock sample and carry the dissolved ions (mainly calcium and carbonate ions) out of the sample. Later, all four parameters stabilize at constant values. The pH drops from near 9, which is the value at equilibrium between the rock and the brine with no CO_2, to near 6. The calcium concentration and alkalinity increase from a value close to zero to about 9.5 mmol L^{-1} L and 19 mmol L^{-1}, respectively, as a result of the calcite dissolution. The fluid electrical conductivity increases from approximately 0.1 S m^{-1} to

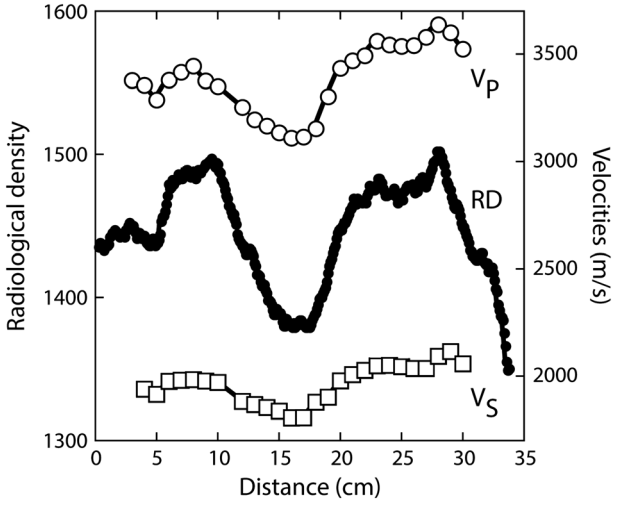

Figure 6. Average values of *P* and *S* wave velocities (V_P and V_S) and radiological density (RD) as a function of position along of the sample. Zero position corresponds to the sample inlet.

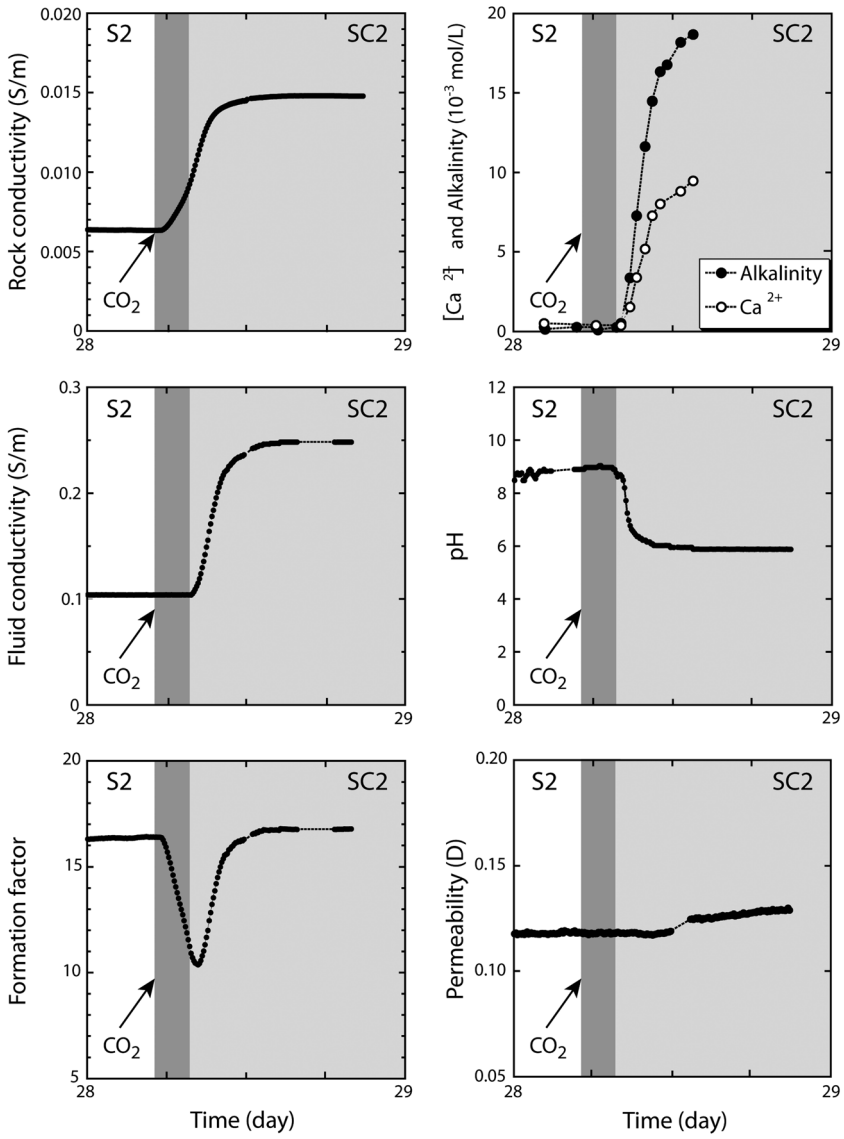

Figure 7. Evolution of the different physical and geochemical parameters monitored during the first day of the second percolation of CO_2-enriched fluid (period denoted SC2).

approximately 0.25 S m^{-1}, as a consequence of increased ion concentrations. The rock electrical conductivity changes earlier than the fluid electrical conductivity, because the rock conductivity is measured between the inlet and the outlet of the sample, where the electrodes are placed, and the fluid conductivity is measured at the outlet of the sample. The rock electrical conductivity begins to rise from its initial value of 6.3×10^{-3} S m^{-1} about 18 min after injection of the CO_2-rich solution begins. The conductivity stabilizes at 14.7×10^{-3} S m^{-1} approximately 6 h after injection begins. Consequently, the formation factor, which is the ratio between the fluid and the rock electrical conductivity, initially decreases (the rock electrical conductivity increases, while the fluid electrical conductivity remains at its initial value); then it increases when the fluid electrical conductivity starts increasing, and it eventually stabilizes at a value close to its initial value, about 16. The sharp downward peak seen in Figure 7 is thus simply an experimental artifact resulting from the way rock and fluid electrical conductivities are measured in situ. The permeability varies little during the first 6 h and then increases very slowly during this first day of the second injection (period SC2).

Table 3 shows, for the three injections, the times at which the rock and fluid electrical conductivities start to depart from their preinjection values, as well as the times required for the stabilization of the electrical conductivities. The corresponding volumes of fluid that have been injected at those times are also specified.

Table 3. T^r_c and T^f_c are the Times for Which the Rock and Fluid Electrical Conductivities, Respectively, Start to Depart From Their Initial Value[a]

Period	T^r_c (min)	V^r_c (L)	T^f_c (min)	V^f_c (L)	T^r_{stab} (min)	V^r_{stab} (L)	T^f_{stab} (min)	V^f_{stab} (L)
SC1	25.1	0.16	159.4	1.01	449.0	2.86	435.3	2.77
SC2	18.7	0.12	133.0	0.85	365.0	2.32	387.0	2.46
SC3	16.3	0.10	133.1	0.85	212.8	1.35	376.3	2.39

[a] V^r_c and V^f_c are the volumes of fluid that have been injected at these times. T^r_{stab} and T^f_{stab} are the times for which the conductivities of the rock and of the fluid, respectively, become constant. V^r_{stab} and T^f_{stab} are the volumes of fluid injected at these times.

In the case of the first injection (SC1), the effects on the fluid electrical conductivity are visible after 159.4 min, a time closed to the residence time of the fluid in the sample (equal to 155.8 min). For the second (SC2) and the third (SC3) injections, the times are shorter and shorter, suggesting that preferential pathways have been developed. Similarly, the times required for obtaining a constant value of the different parameters decreases with each percolation experiment.

3.3. Long-Term Behavior

The evolution of the different parameters measured during the entire second (periods S2 and SC2) and third (periods S3, SC3, and DC3) percolations are represented in Figure 8. During the period SC2 (percolation of

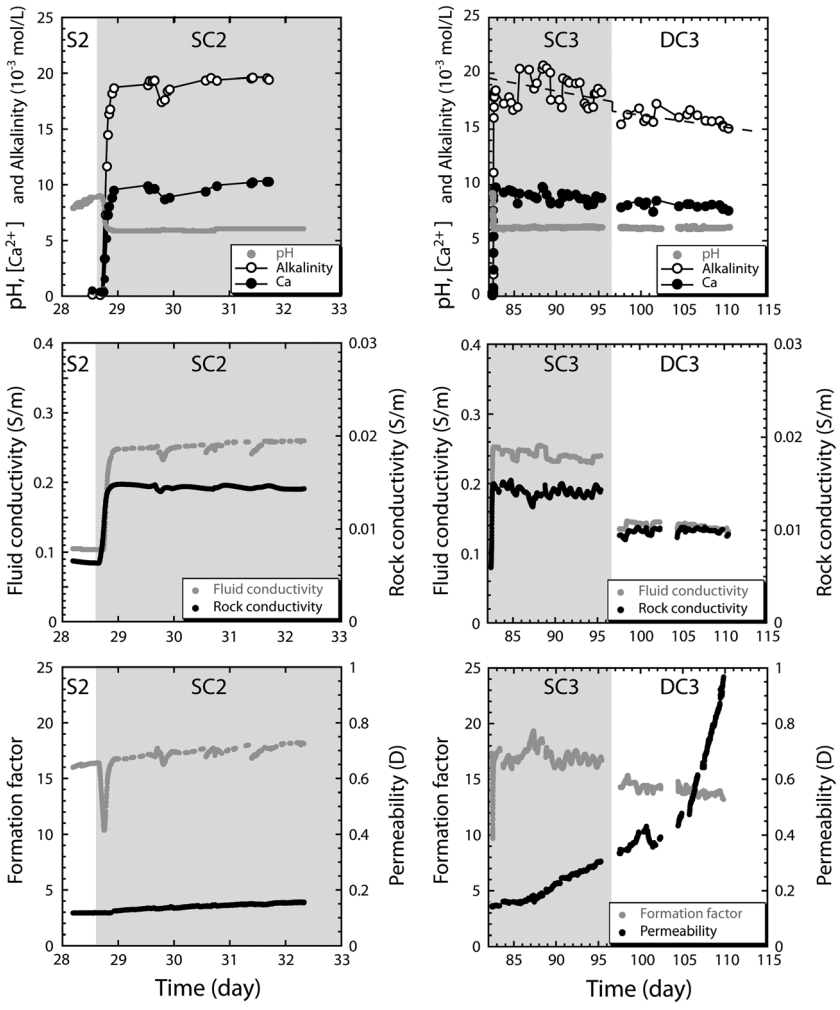

Figure 8. Evolution of the different physical and geochemical parameters monitored during the second percolation (periods S2 and SC2) and the third percolation (periods S3, SC3, and DC3).

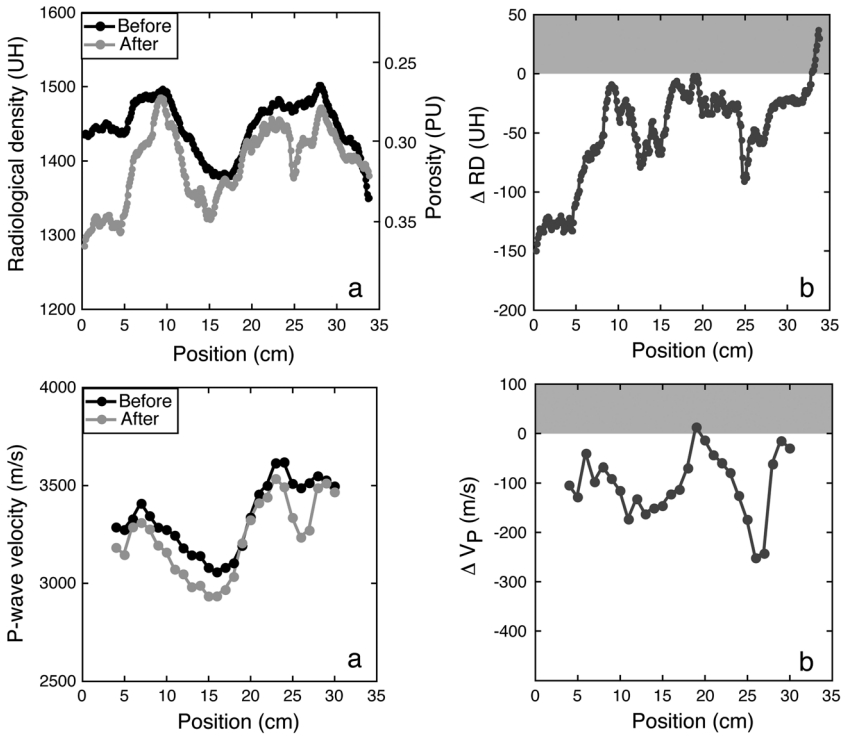

Figure 9. (a) Radiological density, in HU, and porosity, in PU, on the secondary *y* axis, after (in grey) and before (in black) the percolation experiments, along the main axis of the sample. (b) Variation of the radiological density (ΔRD) between the beginning and the end of the percolation experiments, along the main axis of the sample (100 UH corresponds to about −0.05 PU). (c) Ultrasonic *P* wave velocity after (in gray) and before (in black) the percolation experiments, along the main axis of the sample. (d) Variation of the ultrasonic *P* wave velocities, between the beginning and the end of the experiment, along the main axis of the sample.

CO_2-rich brine), which lasted 4 days, the conductivity of the rock decreased slightly, whereas the conductivity of the fluid increased. As a consequence, the electrical formation factor increased (by 14%) during this period. The permeability increased uniformly (by 32%). The alkalinity and the calcium concentration showed slight, steady increases (after the initial rapid increase), from 19 mmol L^{-1} to 20.5 mmol L^{-1} and from 9.5 mmol L^{-1} to 10.5 mmol L^{-1}, respectively. The pH stayed relatively constant, at a value close to 6.

During the period SC3 of the third percolation (percolation of the CO_2-rich brine), the pH of the fluid remained at a mean value of 6.18, like in the previous percolation (period SC2). The alkalinity and calcium concentration showed slight, steady decreases, from 20.5 mmol L^{-1} to 18 mmol L^{-1} and from 10.5 mmol L^{-1} to 9 mmol L^{-1}, respectively. Consequently, and contrary to the period SC2, the fluid electrical conductivity slightly decreased (by 5%), leading to a slight decrease in the formation factor (by 11%, from 17.5 to 15.5). The permeability continued to increase at an increasing rate.

When the percolating fluid switches from CO_2-rich brine to CO_2-rich distilled water with the same pH (period DC3), the main effect on the fluid is a sudden decrease in its electrical conductivity, from 0.24 S m^{-1} at the end of the period SC3 to 0.14 S m^{-1} at the beginning of the period DC3, since the injected fluid lacks the sodium and chloride ions that were present in the brine. The rock electrical conductivity also slows a sharp decrease, from 0.015 S m^{-1} at the end of the period SC3 to 0.010 S m^{-1} at the beginning of the period DC3. As a result, the formation factor shows only a small decrease at the SC3-DC3 transition (from 16 to 15). Alkalinity and calcium concentration values decrease at a slightly higher rate than with the brine, as indicated by Figure 8 (dashed line).

During the period DC3, as during the period SC3, alkalinity, calcium concentration, formation factor, and fluid electrical conductivity continue to slowly decrease, while the pH remains constant at a mean value of 6.15. The permeability continues to increase more rapidly to reach 1 D at the end of the experiment.

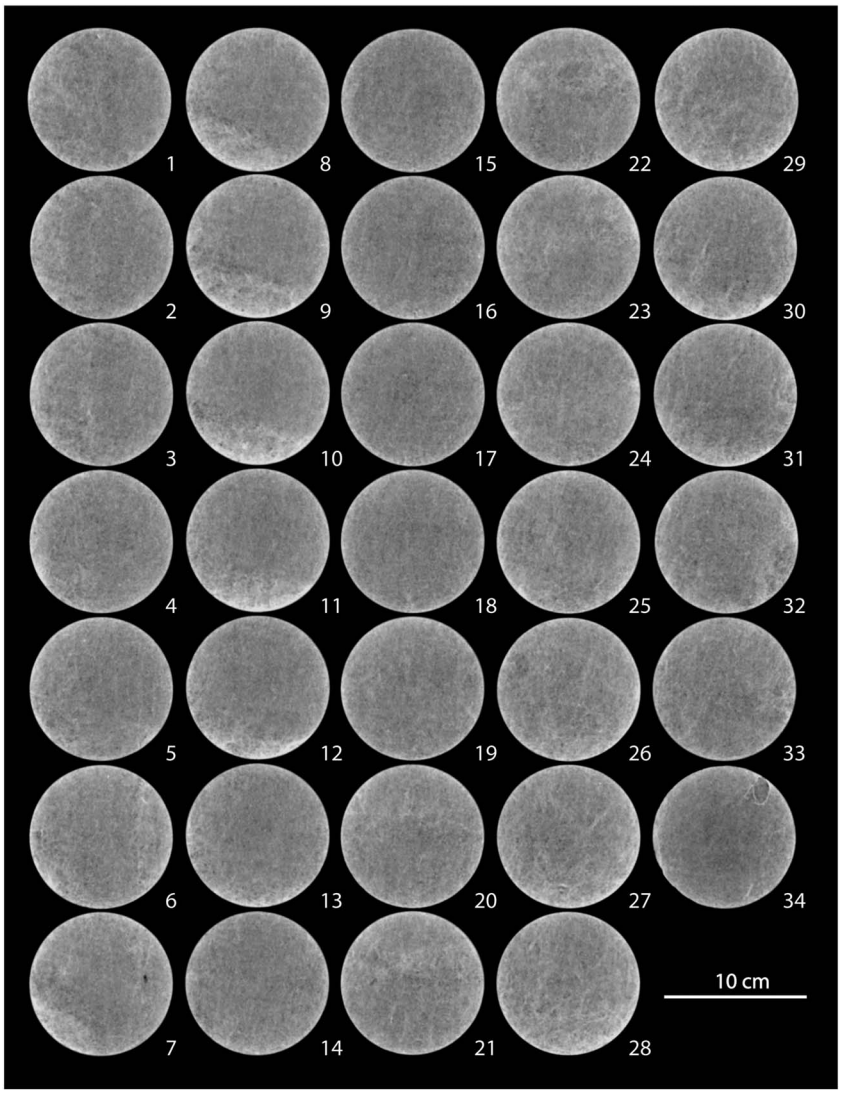

Figure 10. Maps obtained by X-ray tomography, before the percolation experiments. Pale grey zones are dense zones of low porosity. The number indicates the position (in centimeter) along the main axis of the sample.

Unlike calcium ions and the ions from the carbonate system, other ion concentrations are very low, as detected by ionic chromatography. Magnesium is the only other ion whose concentration varies significantly upon injection of the CO_2-rich fluid; its concentration increases form 3.7 μmol L^{-1} to about 100 μmol L^{-1}.

3.4. Sample Properties After the Experiment

The same characterizations as the ones performed before the percolation experiments were repeated when the sample was removed from the experimental device. The permeability measured after the experiment was 0.970 ± 0.024 D.

Figure 9a shows how the radiological density changed during the experiment. To better appreciate its evolution, we subtracted the initial profile from the final one (Figure 9b). We observe that the radiological density decreased over almost the whole length of the sample, except for the last centimeter, for which it increased. The average reduction is 3.4%. The reduction is important (approximately 9%) in the first 5 cm of the sample (corresponding to the inlet) and of variable intensity afterward. For example, it is almost null around 19 cm but is 6% around 25 cm. This heterogeneous behavior is also visible in the maps obtained from X-ray tomography before (Figure 10) and after (Figure 11) the experiment. For example, the maps 17 to 19

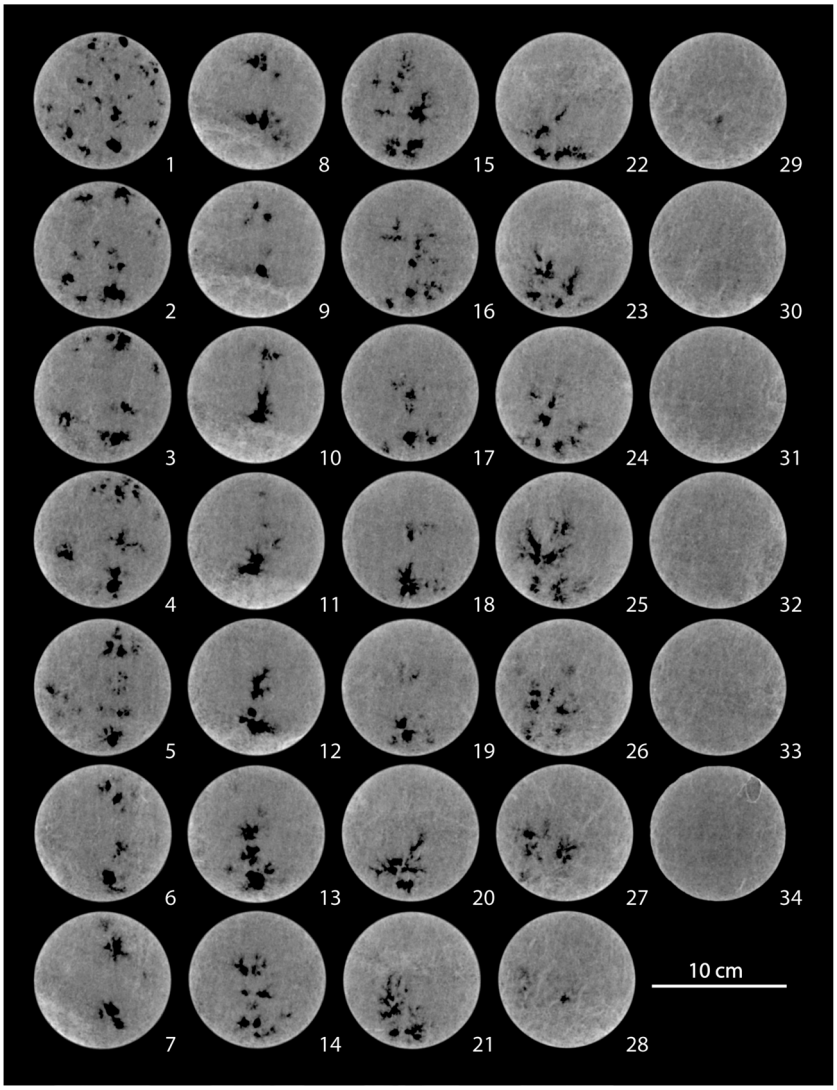

Figure 11. Maps obtained by X-ray tomography, after the percolation experiments. Dark zones are porous zones. The number indicates the position (in centimeter) along the main axis of the sample.

show fewer dark zones than maps 14 to 16. These maps suggest that dissolution was more active in the areas where the initial radiological density was low: the zones that are pale grey, for example in the maps 8 to 12 before the experiment, are always present after the experiment, but the surrounding zones have dissolved. As a result, the sample shows localized dissolutions. Figure 12 is a 3-D reconstruction of the porosity created by the dissolution of the rock. It has been obtained by subtracting the CT scans acquired after percolation from the ones collected before. We observe that the dissolution took the form of wormholes, very finely ramified. By the end of the experiment, the main wormhole had spread through almost the entire length of the sample (~30 cm). It bypassed the denser zone (located between 5 and 12 cm) shown in the maps of Figure 10 (light gray). The fact that the radiological density increased close to the outlet of the sample may suggest that the dissolved calcite had accumulated and reprecipitated there. Scanning electron microscope and cathodoluninescence imaging could not help in distinguishing the eventual reprecipited calcite from the original one. Addition of a trace element like manganese in the injected brine would have given a distinct orange luminescence [*Amieux*, 1982].

After the percolation experiments, measurements of the *P* and *S* wave velocities in a dry state could not be performed on the totality of the sample because some zones were too porous, leading to high-attenuation and poor-signal quality. Measurements of *P* wave velocities could however be realized in the fluid-saturated

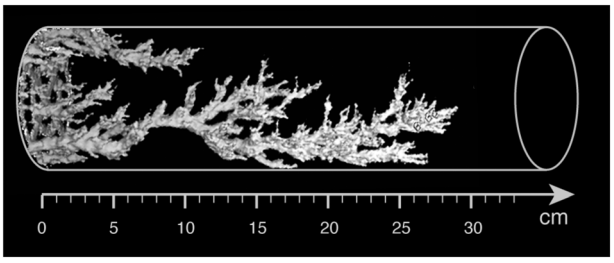

Figure 12. Three-dimensional reconstruction, from X-ray tomography, of the porosity created by calcite dissolution induced by injection of CO_2-saturated fluids in the studied carbonate sample. It shows the formation of a ramified wormhole with a main channel. This image has been obtained by subtracting the CT scans acquired before the injections from the CT scans acquired after.

rock sample immediately after the experiment. For almost the entire length of the sample, fluid-saturated *P* wave velocities were lower after the percolation experiments than before injection (Figures 9c and 9d). But, as observed for the radiological density, the magnitude of the decrease varies along the sample: it is a maximum at position 27, where the *P* wave velocities have dropped by 270 m s^{-1} (i.e., a relative decrease of 8%), and there is no decrease at position 19. Qualitatively, the decrease in the radiological density and that of the *P* wave velocity are correlated (Figures 9b and 9d). Note that the velocities could not be measured at the position 34, for which an increase in the radiological density was observed, because of the presence of the endcaps that help maintain the sample on the experimental device.

The volume of the electrical percolation threshold after experiment, obtained by miscible displacement experiments (Figure 13), is 0.03 and the stability volume is greater than 16, meaning that the heterogeneity of the sample has increased. The electrical formation factor, the cementation factor, and the electrical tortuosity are 13.3 ± 0.3, 2.2, and 2.0, respectively (Table 4).

4. Interpretation and Discussion

4.1. Evidence of Calcite Dissolution

The evolutions of the different parameters (the decrease of the radiological density and of the electrical formation factor, the increase of the calcium concentration and of the alkalinity, and the decrease of the pH to a stabilized value of 6 during the percolation of the acidified fluid) clearly indicate dissolution of the calcite that composes the rock sample. Within the range of measured pH, the dissolution can be written as

$$CaCO_3 + CO_2 + H_2O \leftrightarrow Ca^{2+} + 2HCO_3^- . \quad (9)$$

In the range of considered pH (approximately 6), the principal ion of the carbonate system is HCO_3^-; as a consequence, the alkalinity is reduced by the concentration of this ion and, according to equation (10), should be twice the calcium concentration, which is what we observed (Figure 8).

The ionic strength (Figure 14) for the second and third percolation is always less than 0.1 mol L^{-1}, which validates, a posteriori, the expression used in equation (7). We notice that for each percolation of the acidified

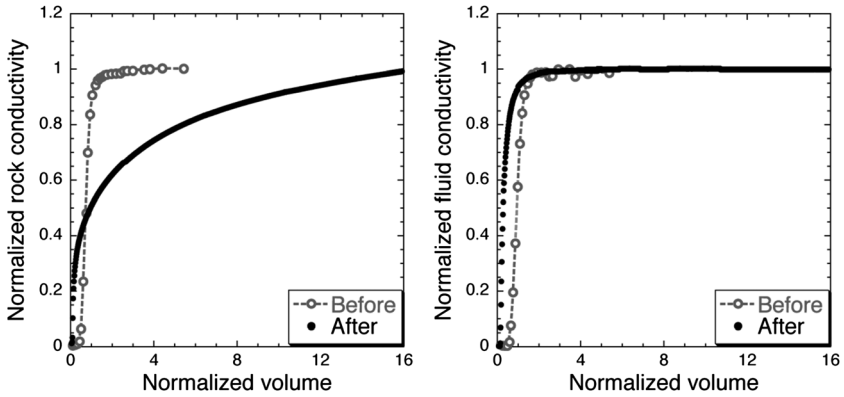

Figure 13. Comparison of the curves obtained from miscible displacement experiments performed on the carbonate sample, before and after the injection experiments. The electrical conductivities (left) of the rock and (right) of the fluid, normalized to their final values, are plotted as a function of the number of pore volumes of fluid injected.

Table 4. Porosity (ϕ), Permeability (k), Electrical Percolation Threshold (EPT), Stability Volume (SV), Electric Formation Factor (F), Cementation Factor (m), and Electric Tortuosity (τ_e) Measured Before and After Experiment[a]

	ϕ (%)	k (D)	EPT	SV	F	m	τ_e
Before	28.6	0.120	0.30	2.2	15.7	2.20	2.12
After	30.7	0.970	0.03	16	13.3	2.19	2.02

[a]The porosity after the experiment is obtained using the mass of the dissolved calcite.

fluid (periods SC2, SC3, and DC3), the ionic strength remains relatively constant after a short time of stabilization. Its value is imposed by the chemical composition of the injected fluid (brine with 10^{-2} mol L^{-1} of NaCl for the periods SC2 and SC3 and distilled water for the period DC3) and by the calcite dissolution bringing calcium and carbonate ions into solution.

The degree of saturation of calcite, Ω, shown in Figure 15 for the second and third percolations, remains always less than 1, which means that the system is undersaturated with respect with calcite and that the dissolution is actually thermodynamically possible. The average values of the degree of saturation are 0.75 and 0.85 for the periods SC3 and DC3, respectively, but values as high as 0.95 can be observed (Figure 15 left, period SC3). Furthermore, these values are average values for the whole core sample and not local values. It is thus possible that the degree of saturation may be locally larger than 1, in particular in the zones where the fluid is more "stagnant," outside the main flow paths. In these zones, calcite precipitation can occur.

4.2. Dominant Mechanism

The evolution of the studied system, and in particular the dissolution pattern, depends on the magnitude of the different processes involved in the reaction and transport mechanism (i.e., kinetics, advection, dispersion, and molecular diffusion). Experimental and theoretical studies have shown that dimensionless numbers are useful criteria for determining the different dissolution regimes [e.g., *de Marsily*, 1986] and subsequently the generated pattern of dissolution [e.g., *Golfier et al.*, 2002]. The Péclet number, which compares the magnitude of hydrodynamic dispersion relative to molecular diffusion, is given by *Oelkers* [1996]:

$$P_e^* = \frac{d\ v_{df}}{D}, \tag{10}$$

where d is the average grain diameter, D is the mass diffusion coefficient, and v_{df} is the pore flow rate (obtained by $v_{df} = Q/S\phi$, with S the cross-section area of the sample). With d between 500 μm and 1 mm, $v_{df} = 3.7 \times 10^{-5}$ m s^{-1} and $D = 10^{-9}$ m^2 s^{-1} (the standard value for calcium at 25°C), the values for Pe^* ranges from 18.5 (for the smaller grains) to 37 (for the larger ones), meaning that hydrodispersion dominates molecular diffusion [*Bear*, 1969].

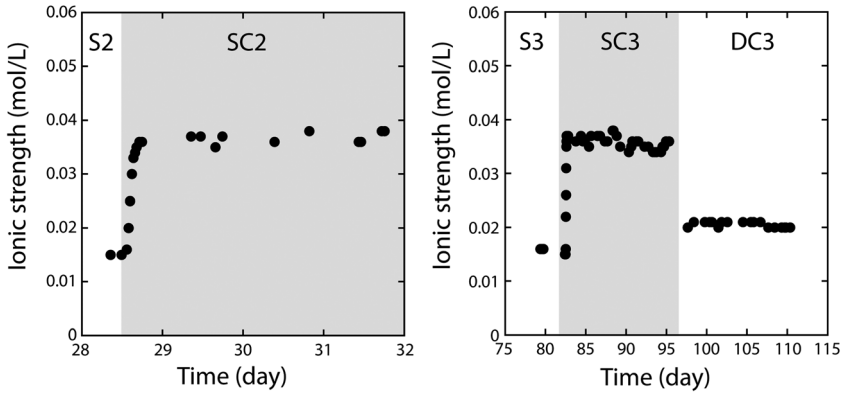

Figure 14. Ionic strength as a function of time, during injection 2 (periods S2and SC2) and injection 3 (periods S3, SC,3 and DC3), respectively.

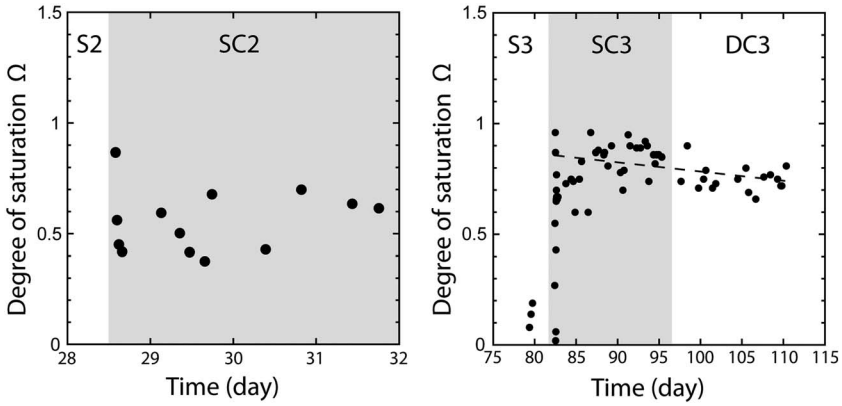

Figure 15. Evolution of the degree of saturation of calcite, Ω, during injection 2 (periods S2 and SC2) and injection 3 (periods S3, SC3, and DC3), respectively.

For such values, the coefficient of longitudinal hydrodynamic dispersion D_L can be approximated by the following empirical expression, proposed by *Bear* [1969] (rigorously for the case of homogeneous media):

$$D_L = D\ \kappa\ (P_e)^{n_\kappa}, \tag{11}$$

in which κ and n_κ are constants equal to 0.5 and 1.2, respectively, since Pe^* is here less than 100.

The obtained values for D_L range from $1.66 \times 10^{-8}\ m^2\ s^{-1}$ to $3.81 \times 10^{-8}\ m^2\ s^{-1}$, which is more than 1 order of magnitude higher than the mass diffusion coefficient D.

By replacing, in equation (10), the grain size d by the characteristic length of the studied system L_c and D by D_L, we obtain the so-called hydrodynamic Péclet number, Pe_D, which compares the magnitude of the advection to the hydrodynamic dispersion [*Catchpole and Fulford*, 1966]:

$$P_{e,D} = \frac{L_c\ v_{df}}{D_L}. \tag{12}$$

With $L_c = 3.47 \times 10^{-1}$ m (the length of the core), the values obtained for Pe_D are between 773 (for the smallest grains) and 337 (for the largest ones). It means that advection dominates dispersion.

The next dimensionless number useful for the work presented here is the Damköhler number, *Da*, which compares the relative importance of the reaction rate versus the advection rate. It can be obtained by [*Knapp*, 1989]

$$D_a = \frac{\alpha\ S_r\ k(T)\ L}{C_{eq}\ v_{df}}, \tag{13}$$

where α is the stœchiometric coefficient of Ca in calcite $CaCO_3$ ($\alpha = 1$), S_r is the reactive specific surface area (in $m^2_{minéral}\ m^{-3}_{solution}$), $k(T)$ is the dissolution rate constant of calcite at the temperature T (in $mol\ m^{-2}\ s^{-1}$), and C_{eq} the concentration of Ca^{2+} at equilibrium with the calcite (in $mol\ L^{-1}$).

With $Sr = 4.69 \times 10^4\ m^{-1}$ [*Clavaud*, 2001], $k(25°C) = 6.1 \times 10^{-5}\ mol\ m^{-2}\ s^{-1}$ (evaluated with the formalism of *Plummer et al.* [1978], in the case of a fluid having a partial pressure in CO_2 of 1 atm, leading to a pH equal to 3.9) and $[Ca^{2+}] = 7.86 \times 10^{-3}\ mol\ L^{-1}$ (calculated with the help of geochemical code PHREEQC 2.0 [*Parkhurst and Appelo*, 1999] for an injected fluid having a p_{CO2} of 1 atm and $NaCl = 10^{-2}\ mol\ L^{-1}$), D_a is equal to 3486. It thus means that reaction rates are here higher than advection rates and that the dissolution is here transport controlled. Note that the reactive specific surface area *Sr* in equation (20), is different from the specific surface area (defined as the total pore surface area divided by the sample volume); S_r is the fraction of the specific surface area in contact with the reactive fluid and chemically reactive. The difference can be especially large [e.g., *Noiriel et al.*, 2009; *Gouze and Luquot*, 2011], in the case of fluid-channeling phenomena, which can decrease the reactive specific surface area by several orders of magnitude compared to the specific surface area

Table 5. Porosities Obtained, Before and After Experiment, by the Different Methods Utilized[a]

	ϕ_{CaCO3}	ϕ_F	ϕ_{DR}
Before	0.286	0.284	0.286
After	0.310	0.309	0.310
$\Delta\phi$	0.024	0.025	0.024

[a]The ϕ_{CaCO3} denotes the porosity obtained using the masse of the dissolved calcite. The porosity ϕ_F is calculated from the electric formation factor using the Archie law. The porosity ϕ_{DR} is obtained from the radiological density.

[*Oelkers*, 1996]. In this case, the reactive fluid is isolated from the bulk of the potential reactive surfaces. Second, it is likely that the reactive specific surface area changes with time during the percolation experiments; calcite dissolution may decrease the surface roughness, thus decreasing the pore surface area. Conversely, the special case of surface-controlled dissolution can increase the surface relief in the form of step-like features [*Berner and Morse*, 1974], and fluid channeling can also increase reactive-specific surface area in preferred flow paths.

The pattern of dissolution (see Figure 12) is nevertheless in tune with high values for Pe_D and *Da*. *Golfier et al.* [2002] have defined five types of dissolution patterns according to the values of Pe_D and *Da:* for Pe_D more than about 2×10^{-2} and *Da* more than about 8×10^{-3}, the dissolution is called "wormhole dominant."

In a very active hydrodynamic flow, the heterogeneous pore network guides the flow along particular pathways. As a consequence, the aqueous solution in these channels and the stagnant solution in poorly connected regions or pore dead ends can have different saturation states with respect to the minerals. Even if the rock is globally being dissolved, some precipitations may occur in the more stagnant areas, as was suggested earlier.

The fact that dissolution is controlled by mass transport is also clearly visible in the temporal evolution of the permeability. At the beginning of the percolation experiment, the dissolution mainly happens at the inlet of the sample, which does not contribute to increasing the permeability of the sample (cf. period SC2 and beginning of period SC3 in Figure 8). During the first 87 days, the permeability slightly decreases as a result of the transport of the fines (i.e., micritic grains) that may clog the pores at the outlet of the sample [*Noiriel et al.*, 2005]. Then, from day 87 to day 100, permeability increases more and more as the number of pores that participate in flow increases and as the wormhole spreads upward. After day 100, when the main wormhole is near the outlet of the sample, the permeability increases dramatically.

4.3. Porosity Change

The porosity of the sample after the percolation experiments can be calculated in different ways: (1) from the mass of the dissolved calcite (equation (8)), integrated over all the percolation periods; (2) from the electric formation factor, using Archie's equation (equation (2)); and (3) from the radiological density, using a calibration coefficient.

Table 5 reports the values obtained by these different techniques. A constant cementation coefficient of 2.2 has been used in Archie's equation. We notice a very good agreement between the porosity values obtained from the fluid chemistry, Archie's equation and the radiological density (ϕ_{CaCO3}, ϕ_F, and ϕ_{DR}, respectively).

4.4. Permeability-Porosity Relationships

The variations of permeability as a function of porosity are plotted in Figure 16 for the periods SC2, SC3, and DC3. The porosity values reported in this graph are the values obtained from the calcium released during the experiment (denoted ϕ_{CaCO3} in Table 5). Two power laws connecting permeability and porosity can be inferred from the data. During the periods SC2 and SC3, the permeability is proportional to ϕ^{19}, and during the period DC3, permeability is proportional to ϕ^{56}. The values of the power laws exponents are here very high, but high values have already been reported by *Mc Cune et al.* [1979], *Noiriel et al.* [2005], or *Smith et al.* [2013], for carbonate samples showing a heterogeneous initial microstructure. The values are though different from sample to sample, depending on the rock type and the degree of heterogeneities. If the same experiment were to be conducted on the same type of carbonate than the one studied here, one would expect the exponents to have values close to the ones found here, but not necessary exactly the same, since the dynamics of wormhole formation are highly nonlinear, and small differences in the rock microstructure may lead to different evolution of the instable reaction front. The change in the exponent, from 19 for the periods

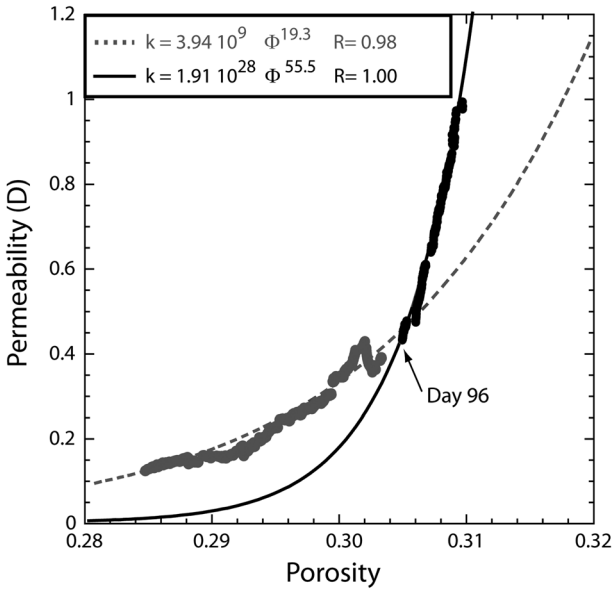

Figure 16. Evolution of permeability as a function of porosity during the periods S2, SC2, and SC3 (grey symbols), and period DC3 (black symbols).

SC2 and SC3 to 56 for the period DC3, may suggest a change in the geometry of the wormhole: as the dissolution progresses and leads to the formation of the wormhole, the reactive fluid is focused into the main flow path(s), which has the effect of decreasing the reactive area and consequently the Damköhler number. According to *Golfier et al.* [2002], the initial value of the reactive surface area is in tune with a "dominant wormhole" pattern, but if the reactive surface area decreases, the dissolution structure can evolve toward a "ramified wormhole." If the experiment had been conducted until the wormhole had reached the outlet boundary, the permeability would have increased more, reaching several darcys, but if the development of the wormhole keeps the same geometry, one would expect the same exponent of 56 in the permeability-porosity power law relationship. As observed by *Smith et al.* [2013], high and time-dependant values of the power law exponent are needed to accurately capture the effects of fast pathway development in heterogeneous carbonate samples.

As shown theoretically [e.g., *Daccord et al.*, 1993; *Békri et al.*, 1995; *Algive et al.*, 2012], the dissolution regime is a key factor that controls the k-ϕ relationships. In transport-limited dissolution processes, where convection is predominant (i.e., $PeDa > 1$ and $Pe > 1$, as in the work presented here), numerical simulations using different approaches (such as random walks, finite difference formulations, and pore network modeling) and performed on various classes of media, from deterministic to random, have all shown that the wormhole effect occurs. In that case, dissolution occurs along the preferential paths of convective fluid, which has a maximum impact on permeability, compared to the other dissolution regimes. The curve of permeability versus porosity is then concave up [*Békri et al.*, 1995]. A plateau is first observed, and the permeability increases rapidly later on, as seen in Figure 16. *Noiriel et al.* [2005] experimentally illustrated a concave down curvature of the permeability-porosity curve, since the dissolution processes were in that case surface-limited (low D_a), which was also numerically obtained [*Békri et al.*, 1995]. Adequate permeability-porosity relationships are essentials in reservoir-scale simulation in order to correctly predict changes in porosity and permeability, in various applications such as acid stimulation or geologic carbon storage. As pointed out in *Carroll et al.* [2013], the scaling of these relationships from the laboratory scale to the reservoir scale are far from being straightforward and depend on the ability of the laboratory-scale core to capture enough heterogeneities representative of the reservoir.

5. Concluding Remarks

The percolation of CO_2-rich fluids in a carbonate core plug promotes the dissolution of the calcite composing the rock sample, affecting the chemistry of the percolating fluid, the rock microstructure, and the monitored geophysical parameters. The dissolution of the rock is rapidly (after the injection of about one pore volume) and clearly seen in the geochemical parameters monitored at the sample outlet (calcium concentrations, pH, and alkalinity) as well as in the electrical conductivity of the outstream fluid. The dissolution of the rock is heterogeneous, with the formation of wormholes visible on the 3-D reconstructions of the pore system from μ-CT imaging. With our experimental conditions (in particular, the pH of the injected fluid, flow rate and sample size, mineralogical composition, and petrophysical properties), the regime of dissolution corresponds to a transport-limited regime, for which both D_a and Pe are greater than 1. Various theoretical and numerical works have predicted that in this case dissolution is mostly localized along the main flow paths and is more important at the upstream end of the sample, which we have experimentally confirmed in this work. Furthermore, the

observed evolution of permeability as a function of porosity, an increasing curve with an increasing derivative (concave up), is consistent with previous numerical studies for such a dissolution regime. This study shows that nonseismic geophysical techniques (i.e., electrical measurements) are promising in the monitoring of the impact of the geochemical changes within the subsurface on the geophysical parameters.

Acknowledgments
The authors are grateful to Jean-Pierre Delhomme and Olivier Lopez for fruitful discussions. Ionic chromatography was performed by Caroline Gorge at the Laboratoire de Géochimie et Cosmochimie (IPG, Paris). This research was supported by CNRS-INSU programs ACI Eau-Environnement, program ECCO, and Schlumberger Water Services. The authors want to thank the Associate Editor and two anonymous reviewers for their comments and suggestions. This is IPG contribution 3497.

References

Abdel Aal, G., E. Atekwana, S. Radzikowski, and S. Rossbach (2009), Effect of bacterial adsorption on low frequency electrical properties of clean quartz sands and iron-oxide coated sands, *Geophys. Res. Lett.*, *36*, L04403, doi:10.1029/2008GL036196.

Algive, L., S. Békri, F. H. Nader, O. Lerat, and O. Vizika (2012), Impact of diagenetic alterations on the petrophysical and multiphase flow properties of carbonate rocks using a reactive pore network modeling approach, *Oil Gas Sci. Technol.*, *67*(1), 147–160.

Amieux, P. (1982), La cathodoluminescence: Méthode d'étude sédimentologique des carbonates, in *Bulletin des Centres de Recherches Exploration-Production*, vol. 6, pp. 437–483, Elf-Aquitaine, France.

André, L., M. Azaroual, A. Menjoz, C. Kervévan, J. M. Lombard, and P. Egermann (2007), Control of supercritical CO_2 injectivity in the deep Dogger aquifer of the Paris Basin from different injection scenarios, Presented at the First French-German Symposium on Geological Storage of CO_2, Potsdam, Germany, 21–22 June 2007.

Back, W., B. B. Hanshaw, T. Y. Pyle, L. N. Plummer, and A. E. Weidie (1979), Geochemical significance of groundwater discharge and carbonate solution to the formation of Caleta Xel Ha, Quintana Roo, Mexico, *Water Resour. Res.*, *15*(6), 1521–1535, doi:10.1029/WR015i006p01521.

Bazin, B. (2001), From matrix acidizing to acid fracturing: A laboratory evaluation of acid/rock interactions, *SPE Prod. Facil.*, *16*(1), 22–29, doi:10.2118/66566-PA.

Bear, J. (1969), Hydrodynamic dispersion, in *Flow Through Porous Media*, edited by R. J. M. De Wiest, pp. 109–199, Academic Press, New York.

Békri, S., J. F. Thovert, and P. M. Adler (1995), Dissolution of porous media, *Chem. Eng. Sci.*, *50*(17), 2765–2791, doi:10.1016/0009-2509(95)00121-K.

Berner, R. A., and J. W. Morse (1974), Dissolution kinetics of calcium carbonate in sea water. IV. Theory of calcite dissolution, *Am. J. Sci.*, *274*(2), 108–134, doi:10.2475/ajs.274.2.108.

Birch, F. (1960), The velocity of compressional waves in rocks to 10 kilobars, part 1, *J. Geophys. Res.*, *65*, 1083–1102, doi:10.1029/JZ065i004p01083.

Bravo, H. A., R. A. Soto, R. E. Sosa, P. A. Sanchez, A. L. J. Alarcon, J. Kahl, and J. B. Ruiz (2006), Effect on acid rain on building material of the El Tajin archaeological zone in Veracruz, Mexico, *Environ. Pollut.*, *144*(2), 655–660, doi:10.1016/j.envpol.2005.12.052.

Carroll, S., Y. Hao, M. Smith, and Y. Sholokhova (2013), Development of scaling parameters to describe CO_2-rock interactions within Weyburn-Midale carbonate flow units, *Int. J. Greenhouse Gas Control*, *16S*, S185–S193, doi:10.1016/j.ijggc.2012.12.026.

Catchpole, J. P., and G. Fulford (1966), Dimensionless groups, *Indust. Eng. Chem.*, *58*, 46–60.

Cederstrom, D. J. (1957), Geology and ground-water resources of the York-James Peninsula, Virginia, U.S. Geological Survey Water-Supply Paper 1361, 237 pp.

Clavaud, J. B. (2001), Etude des propriétés de transport (hydraulique et électrique) des roches. Effets de la microstructure, de la présence de plusieurs fluides, de la fracturation et de l'interaction eau-roche, PhD thesis, Univ. of Paris VII, Paris, France.

Contraires, S. (2008), Effets hydrauliques d'une injection de CO_2 en réservoir souterrain: Mise au point de méthodes géophysiques de surface permettant de suivre ces effets, PhD thesis, Institut de Physique du Globe, Paris, France.

Contraires, S., S. Vialle, M. Zamora, P. Zuddas, and O. Lopez (2007), Geophysical monitoring of CO_2 injections in decimetric limestone samples, *Eos Trans. AGU*, *88*(23), Abstract NS31B-05.

Daccord, G., R. Lenormand, and O. Liétard (1993), Chemical dissolution of a porous medium by a reactive fluid. I. Model for the "wormholing" phenomenon, *Chem. Eng. Sci.*, *48*, 168–178.

Darcy, H. (1856), *Les Fontaines Publiques de la Ville de Dijon*, Dalmont, Paris, France.

De Marsily, G. (1986), *Quantitative Hydrogeology*, Academic Press, New York.

Dullien, F. A. L. (1992), *Porous Media: Fluid Transport and Pore Structure*, Academic Press, San Diego, Calif.

Egermann, P., B. Bazin, and O. Vizika (2005), An experimental investigation of reaction-transport phenomena during CO_2 injection, Paper SPE 93674 presented at the 14th SPE Middle East Oil Show, Bahrain, 12–15 March 2005.

Eriksson, N., and G. Destouni (1997), Combined effects of dissolution kinetics, secondary mineral precipitation, and preferential flow on copper leaching from mining waste rock, *Water Resour. Res.*, *33*, 471–483, doi:10.1029/96WR03466.

Gale, I. N., A. T. Williams, I. Gauss, and H. K. Jones (2002), Elucidating the hydrogeological issues associated with aquifer storage and recovery in the UK, *BGS Commercial Report*, CR/02/156/N 35.

Garrouch, A. A., and M. M. Sharma (1994), The influence of clay content, salinity, stress, and wettability on the dielectric properties of brine-saturated rocks; 10 Hz to 10 MHz, *Geophysics*, *59*(6), 909–917, doi:10.1190/1.1443650.

Golfier, F., C. Zarcone, B. Bazin, R. Lenormand, D. Lasseux, and M. Quintard (2002), On the ability of the Darcy-scale model to capture wormhole formation during the dissolution of a porous media, *J. Fluid Mech.*, *457*, 213–254, doi:10.1017/S0022112002007735.

Gouze, P., and L. Luquot (2011), X-ray microtomography characterization of porosity, permeability and reactive surface changes during dissolution, *J. Contam. Hydrol.*, *120–121*, 45–55, doi:10.1016/j.jconhyd.2010.07.004.

Guichet, X., L. Jouniaux, and J. P. Pozzi (2003), Streaming potential of a sand in partial saturation conditions, *J. Geophys. Res.*, *108*(B3), 2141, doi:10.1029/2001JB001517.

Guichet, X., L. Jouniaux, and N. Catel (2006), Modification of streaming potential by precipitation of calcite in a sand-water system: Laboratory measurements in the pH range from 4 to 12, *Geophys. J. Int.*, *166*, 445–460, doi:10.1111/j.1365-246X.2006.02922.x.

Higgins, C. G. (1980), Nips, notches and the solution of coastal limestone: An overview of the problem with examples from Greece, *Estuarine Coastal Mar. Sci.*, *10*(1), 15–30, doi:10.1016/S0302-3524(80)80046-6.

Hoefner, M. L., and H. S. Fogler (1988), Pore evolution and channel formation during flow and reaction in porous media, *AIChE J.*, *34*(1), 45–54, doi:10.1002/aic.690340107.

Johnson, D. L., and P. N. Sen (1988), Dependence of the conductivity of a porous medium on electrolyte conductivity, *Phys. Rev. B*, *37*(7), 3502–3510, doi:10.1103/PhysRevB.37.3502.

Knapp, R. B. (1989), Spatial and temporal scales of local equilibrium in dynamic fluid-rock systems, *Geochim. Cosmochim. Acta*, *53*(8), 1955–1964, doi:10.1016/0016-7037(89)90316-5.

Langmuir, D. (1971), The geochemistry of some carbonate ground water in central Pennsylvania, *Geochim. Cosmochim. Acta*, *35*(10), 1023–1045, doi:10.1016/0016-7037(71)90019-6.

Le Guen, Y., F. Renard, R. Hellmann, E. Brosse, M. Collombet, D. Tisserand, and J.-P. Gratier (2007), Enhanced deformation of limestone and sandstone in the presence of high pCO_2 fluids, *J. Geophys. Res.*, *112*, B05421, doi:10.1029/2006JB004637.

Luquot, L., and P. Gouze (2009), Experimental determination of porosity and permeability changes induced by injection of CO_2 into carbonate rocks, *Chem. Geol.*, *265*, 148–159, doi:10.1016/j.chemgeo.2009.03.028.

Machel, H. G. (1999), Effects of groundwater flow on mineral diagenesis with emphasis on carbonate aquifers, *Hydrogeol. J.*, *7*(1), 94–107, doi:10.1007/s100400050182.

Mc Cune, C. C., H. S. Fogler, and W. E. Kline (1979), An experimental technique for obtaining permeability-porosity relationships in acidized porous media, *Ind. Eng. Chem. Fundam.*, *18*(2), 188–191, doi:10.1021/i160070a016.

Noiriel, C., D. Bernard, P. Gouze, and X. Thibault (2005), Hydraulic properties and microgeometry evolution accompanying limestone dissolution by acidic water, *Oil Gas Sci. Technol.*, *60*(1), 177–192, doi:10.2516/ogst:2005011.

Noiriel, C., B. Madé, and P. Gouze (2007), Impact of coating development on the hydraulic and transport properties in argillaceous limestone fracture, *Water Resour. Res.*, *43*, W09406, doi:10.1029/2006WR005379.

Noiriel, C., L. Luquot, B. Madé, L. Raimbault, P. Gouze, and J. van der Lee (2009), Changes in reactive surface area during limestone dissolution: An experimental and modelling study, *Chem. Geol.*, *265*(1–2), 160–170, doi:10.1016/j.chemgeo.2009.01.032.

Nougaro, J., and C. Labbe (1955), Etude des lois de l'acidification dans le cas d'un calcaire vacuolaire, *Rev. Fran. Pet.*, *10*(5), 354.

Oelkers, E. H. (1996), Physical and chemical properties of rocks and fluids for chemical mass transport calculations, in *Reactive Transport in Porous Media*, Reviews in Mineralogy, vol. 34, edited by P. C. Lichtner, C. I. Steefel, and E. H. Oelkers, pp. 131–191, Mineral Society of America, Washington D. C.

Ormond, P., and A. Ortoleva (2000), Numerical modeling of reaction-induced cavities in a porous rock, *J. Geophys. Res.*, *105*(B7), 16,737–16,747, doi:10.1029/2000JB900116.

Parkhurst, D. L., and C. A. J. Appelo (1999), User's guide to PHREEQC (version 2)—A computer program for speciation, batch-reaction, one-dimensional transport, and inverse geochemical calculations, *U.S. Geol. Surv. ,Water Resour. Invest. Rep., WRI-99-425*, 312 pp.

Plummer, L. N. (1975), Mixing of sea water with calcium carbonate ground water, *Geol. Soc. Am. Mem.*, *142*, 219–236.

Plummer, L. N., and E. Busenberg (1982), The solubilities of calcite, aragonite and vaterite in CO_2-H_2O solutions between 0 and 90°C, and an evaluation of the aqueous model for the system $CaCO_3$-CO_2-H_2O, *Geochim. Cosmochim. Acta*, *46*(6), 1011–1040, doi:10.1016/0016-7037(82)90056-4.

Plummer, L. N., T. M. L. Wigley, and D. L. Parkhurst (1978), The kinetics of calcite dissolution in CO_2-water systems at 5 to 60°C and 0.0 to 1.0 atm CO2, *Am. J. Sci.*, *278*, 179–216, doi:10.2475/ajs.278.2.179.

Podda, F., and G. Michard (1994), Mesure colorimétrique de l'alcalinité, *C.R. Acad. Sci. Paris*, *319*, série II, 651–657.

Polak, A., D. Elsworth, J. Liu, and A. S. Grader (2004), Spontaneous switching of permeability changes in a limestone fracture with net dissolution, *Water Resour. Res.*, *40*, W03502, doi:10.1029/2003WR002717.

Price, R. M., and J. S. Herman (1991), Geochemical investigation of salt-water intrusion into a coastal carbonate aquifer; Mallorca, Spain, *Geol. Soc. Am. Bull.*, *103*(10), 1270–1279, doi:10.1130/0016-7606(1991)103<1270:GIOSWI>2.3.CO;2.

Rege, S. D., and H. S. Fogler (1989), Competition among flow, dissolution and precipitation in porous media, *AIChE J.*, *35*(7), 1177–1185, doi:10.1002/aic.690350713.

Renard, F., J.-P. Gratier, P. Ortoleva, E. Brosse, and B. Bazin (1998), Self-organization during reactive fluid flow in a porous medium, *Geophys. Res. Lett.*, *25*(3), 385–388, doi:10.1029/97GL03781.

Rezaei, M., E. Sanz, E. Raeisi, C. Ayora, E. Vasquez-Sune, and J. Carrera (2005), Reactive transport modelling of calcite dissolution in the fresh-salt water mixing zone, *J. Hydrol.*, *311*(1–4), 282–298, doi:10.1016/j.jhydrol.2004.12.017.

Sarazin, G., G. Michard, and F. Prévot (1999), A rapid and accurate method for alkalinity measurements in seawater samples, *Water Resour. Res.*, *33*(1), 290–294, doi:10.1016/S0043-1354(98)00168-7.

Sigg, L., W. Stumm, and P. Behra (1994), *Chimie des Milieux Aquatiques*, 2nd ed., Masson, Paris, France.

Singurindy, O., and B. Berkowitz (2003), Evolution of hydraulic conductivity by precipitation and dissolution in carbonate rock, *Water Resour. Res.*, *39*(1), 1016, doi:10.1029/2001WR001055.

Smart, P. L., J. M. Dawans, and F. Wheeler (1988), Carbonate dissolution in a modern mixing zone, South Andros Island, Bahamas, *Nature*, *335*, 811–813.

Smith, M. M., Y. Sholokhova, Y. Hao, and S. A. Carroll (2013), CO_2-induced dissolution of low permeability carbonates. Part I: Characterization and experiments, *Adv. Water Res.*, *62*, 370–387, doi:10.1016/j.advwatres.2013.09.008.

Sterpenich, J., J. Sausse, J. Pironon, A. Gehin, G. Hubert, E. Perfetti, and D. Grgic (2009), Experimental ageing of oolitic limestones under CO2 storage conditions: Petrographical and chemical evidence, *Chem. Geol.*, *265*, 99–112, doi:10.1016/j.chemgeo.2009.04.011.

Tenthorey, E., C. H. Scholz, E. Aharonov, and A. Léger (1998), Precipitation sealing and diagenesis: 1. Experimental results, *J. Geophys. Res.*, *103*(B10), 23,951–23,967, doi:10.1029/98JB02229.

Vanorio, T., C. Scotallero, and G. Mavko (2008), The effect of chemical and physical processes on the acoustic properties of carbonate rocks, *Leading Edge*, *27*(8), 1040–1048, doi:10.1190/1.2967558.

Vanorio, T., G. Mavko, S. Vialle, and K. Spratt (2010), The rock physics basis for 4D seismic monitoring of CO_2 fate: Are we there yet?, *Leading Edge*, *29*(2), 156–162, doi:10.1190/1.3304818.

Vialle, S. (2008), Etude des effets de dissolution (et precipitation) sur les propriétés de transport des roches, PhD thesis, Paris Diderot Univ., Paris, France.

Vialle, S., and T. Vanorio (2011), Laboratory measurements of elastic properties of carbonate rocks during injection of reactive CO_2-saturated water, *Geophys. Res. Lett.*, *38*L01302, doi:10.1029/2010GL045606.

Viles, H. A. (1997), Urban air pollution and the deterioration of buildings and monuments, in *An Environmental Overview*, vol. 1, edited by D. Brune and M. Gwinne, pp. 87–96, John Wiley, New York.

Viles, H. A., and C. A. Moses (1998), Weathering nanomorphologies: Their experimental production and use as indicators of carbonate stones decay, *Q. J. Eng. Geol. Hydrogeol.*, *31*, 347–357, doi:10.1144/GSL.QJEG.1998.031.P4.08.

White, W. B. (1988), *Geomorphology and Hydrology of Karst Terrain*, Oxford Univ. Press, New York.

Wyllie, M. R. J. (1957), *The Fundamentals of Electric Log Interpretation*, Academic Press, New York.

Youssef, S., E. Rosenberg, N. Gland, S. Bekri, and O. Vizika (2007), Quantitative 3D characterization of the pore space of real rocks: Improved μ-CT resolution and pore extraction methodology, Presented at the International Symposium of the Society of Core Analysts Calgary, September 10–12.

Zamora, M., and J. P. Poirier (1990), Experimental study of acoustic anisotropy and birefringence in dry and saturated Fontainebleau sandstone, *Geophysics*, *55*(11), 1455–1465, doi:10.1190/1.1442793.